The Effect of Thermal Treatment on the Characteristics of Porous Ceramic-Based Natural Clay and Chitosan Biopolymer Precursors

Suriati Eka Putri[1,2], Ahyar Ahmad[3,4*], Indah Raya[3], Rachmat Triandi Tjahjanto[5], Rizal Irfandi[6], Harningsih Karim[7], Susilo Sudarman Desa[8], and Abd Rahman[9]

[1]*Doctoral Program, Department of Chemistry, Faculty of Mathematics and Natural Sciences, Hasanuddin University, Jl. Perintis Kemerdekaan Km. 20, Makassar 90245, Indonesia*

[2]*Department of Chemistry, Faculty of Mathematics and Natural Science, Universitas Negeri Makassar, Jl. Daeng Tata, Makassar 90244, Indonesia*

[3]*Department of Chemistry, Faculty of Mathematics and Natural Sciences, Hasanuddin University, Jl. Perintis Kemerdekaan Km. 20, Makassar 90245, Indonesia*

[4]*Research and Development Centre for Biopolymers and Bioproducts, LPPM, Hasanuddin University, Jl. Perintis Kemerdekaan Km. 20, Makassar 90245, Indonesia*

[5]*Department of Chemistry, Faculty of Mathematics and Natural Sciences, Brawijaya University, Jl. Veteran, Malang 65145, Indonesia*

[6]*Department of Biology Education, Faculty of Teacher Training and Education, Universitas Puangrimaggalatung, Jl. Sultan Hasanuddin, Madukkeleng, Sengkang 90915, Indonesia*

[7]*Department of Pharmacy, School of Pharmacy YAMASI, Makassar 90244, Indonesia*

[8]*School of Bio-Chemical Engineering and Technology, Sirindhorn International Institute of Technology, Thammasat University, Pathum Thani 12120, Thailand*

[9]*Inorganic Chemistry, King Fahd University of Petroleum & Minerals, Academic Belt Road, Dhahran 31261, Saudi Arabia*

**** Corresponding author:***

tel: +62-8984917549
email: ahyarahmad@gmail.com

Received: December 19, 2022
Accepted: April 18, 2023

DOI: 10.22146/ijc.80375

Abstract: *This study was conducted to determine the role of thermal treatment on the crystallinity and pore characteristics of porous ceramic, which was prepared from natural clay (NC) and chitosan (CS) biopolymer using the gel casting method. CS was used as an environmentally friendly pore-forming agent. The applied temperature treatment was based on thermal analysis (TGA/DTA) results and followed a sintering temperature of 900 to 1100 °C. The results showed that at sintering temperatures from 900 to 1000 °C, the crystallinities of the ceramic decrease (from 76.06 to 74.06%) and the crystallite size decreases (from 35.71 to 34.47 nm) while the lattice strain increases (calculated from the Full Width at Half Maximum (β) of the diffraction peak). The highest porosity of ceramic occurred at a sintering temperature of 1000 °C of 37.82 ± 0.19, but the formation of heterogeneous microstructure was observed. The resulting pore size for all temperature treatments was almost mesoporous (19.1 Å). Based on the results obtained, it is emphasized that the sintering temperature can be used to adjust the porosity and microstructure of porous ceramics.*

Keywords: *porous ceramic; gel casting; sintering; clay*

■ INTRODUCTION

Porous ceramics have undergone substantial research for a variety of crucial applications, such as gas/liquid filtration, thermal insulation, catalyst support, and drug delivery [1-3]. This is due to several properties possessed by porous ceramics, such as their high melting point, low

thermal conductivity, good chemical inertness, and high specific surface area [4]. Several methods are used to prepare porous ceramic, such as pore-forming agent [5], freeze casting [6-7], gel casting [8-10], foam gel casting [11], sacrificial templating [12], and particle stacking [13]. The gel casting method is the most often utilized of the aforementioned techniques due to its benefits of a simple operating process. However, the industry is reluctant to use the gel casting technique because the most commonly used gel is acrylamide (AM), which is a neurotoxin. Thus, several previous researchers have utilized natural polymers in the fabrication of porous ceramics such as egg white [14-15], rice flour [16-17], cassava starch [18-19], sodium alginate [20], and chitosan (CS) [20-21].

In addition, gel casting of porous ceramics also uses raw materials, which are generally used including synthetic oxides such as alumina, zirconia, nitride, and titania, along with polymers that act as gelling agents and also pore templates [22-24]. These raw materials can be quite expensive, making them unsuitable for large-scale manufacture. At the moment, porous ceramics made from natural minerals, particularly clays, have attracted a lot of attention due to their abundance, good chemical resistance, good mechanical properties, and thermal stability [25-26]. Porous ceramic-based clay can also be used in some of the previously described porous ceramic applications [27]. In this study, we tried to develop the use of natural clay (NC) as a raw material and CS as a gelling agent and pore template.

The selection of CS as a pore template is due to it being renewable that is quite abundant in nature and is environmentally friendly [28]. Several previous studies have reported the use of CS as a pore template in the production of porous ceramics by gel casting. Salomão and Brandi [29] succeeded in producing a new porous filamentous using alumina-CS, and the resulting ceramic can be applied to the process of catalysis, filtration, support for biological tissue growth, and thermal insulation. Further research developing a cylindrical porous ceramic using a different raw material, namely aluminum hydroxide, the obtained results show a fairly high porosity (up to 84%) and a specific surface area (up to 7 m^2/g) [30]. The optimum conditions for the use of CS as a gelling agent have been reported by Bengisu and Yilmaz [31] using alumina and zirconia as the raw materials, obtaining the optimum pH for gelification of CS in the slurry at pH 4, reaction temperature 55 °C, the acetic acid concentration of 1 wt.%, and CS concentration of 10 wt.%.

With this perspective, this study has successfully employed NC and CS to prepare an environmentally porous ceramic membrane that has not been previously reported. The porosity of the ceramic body comes from the thermal degradation of CS, which can be easily decomposed in the temperature range of 219–505 °C [30]. A previous study has shown that the sintering temperature significantly affects the characteristics of porous ceramics. Salomão and Brandi [29] reported that thermal treatment affects mechanical strength, porosity, specific surface area and microstructure of gel casting porous ceramics with alumina and CS as raw materials. For instance, low-temperature sintering can make ceramic materials more porous and increase the pore size [32]. However, with a high sintering temperature, the mechanical properties can be improved [33]. The effect of thermal treatment on the microstructure and porosity of porous ceramics based on NC and CS is described in this work due to the major impact of the sintering temperature treatment.

■ EXPERIMENTAL SECTION

Materials

The materials used in this study consist of NC obtained from South Sulawesi (was slightly ground and sieved to pass 60 Mesh, then characterized using XRF, SAA with BET method, and PSA, the characterization results shown in Table 1), CS powder from our previous study [34] (the characteristic shown in Table 1), alumina (Merck, Germany CAS number 1344-28-1), carboxymethyl cellulose (CMC) food grade as a dispersant, and CH_3COOH (99% purity Merck, Germany).

Instrumentation

The instruments used in this study involved furnace (Nabertherm LT 5/14/B410), X-ray fluorescence (XRF, Thermo Fischer Scientific), X-ray diffractometer (XRD,

Table 1. Raw materials used in this study

Natural clay	
Chemical analysis (using XRF; wt.%)	SiO_2: 59.33; Al_2O_3: 2.77; Fe_2O_3: 0.77; CaO: 0.30; TiO_2: 3.84; ZrO_2, NiO, CuO, ZnO, and etc < 0.70
Specific surface area (BET method; $m^2\ g^{-1}$)	17.02
Particle size (using PSA; μm)	4.34
Chitosan	
Molecular weight (kDa)	302.40
Particle size (using PSA; μm)	1.22
Polydispersity Index	0.51
Deacetylation degree (%)	93.81
Loss of ignition (%)	0.71
Moisture regains (%)	8.75
Viscosity (mPa.s)	155.31

Shimadzu 7000), particle size analyzer (PSA, Malvern Panalytical), TGA/DTA (Hitachi STA7300), surface area analyzer (SAA, type Quantachrome Nova 4200e), and scanning electron microscope (SEM, JEOL-6000PL).

Procedure

Specimen preparation

Porous ceramic-based NC and CS were fabricated by the gel casting method. The CS gel (10 wt.% in 0.1 M acetic acid solution, pH 4) was stirred at 40 °C for 2 h until the polymer was completely dissolved [30]. Furthermore, the formation of organoclay through clay modification with CMC (hereinafter referred to as modified clay (MC)) facilitates the interaction between clay and CS [35]. The raw material (clay and alumina with a ratio of 1:1 wt.%, the addition of alumina aims to restrain the rate of thermal expansion of silica, which is the main content in NC [36]) and 0.1 wt.% of CMC dispersant were added to 1.5 mL of distilled water, stirred for 1 h. The CS solution and MC solution were mixed and stirred for 15 min to produce a slurry, and then a 25 × 25 × 120 mm^3 PVC mold was used to pour into and permitted to dry in an air atmosphere for 12 h. The gelled ceramics were molded; the resulting ceramic body is called gel casted green body ceramic. Then sintered with the heating rate based on the results from the analysis of thermal using TGA/DTA with sintering temperature variations of 900, 1000, and 1100 °C for 3 h. An illustration of specimen preparation is shown in Fig. 1.

Determination of heat treatment parameters in gel casted green body ceramic

TG-DTA studies on the Hitachi STA7300 were used to simultaneously determine the heat treatment parameters of gel casted green body ceramic. Gel casted green body ceramic were ground into powder and weighed about 3.9 mg on an alumina crucible for comprehensive thermal analysis and then heated to 1000 °C in a static air environment after being isothermally heated at 30 °C for 10 min under airflow (8 L/min). The alumina was

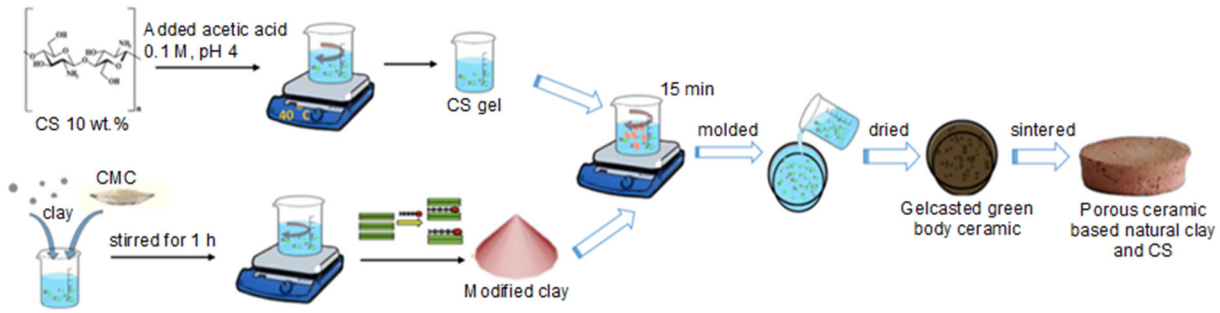

Fig 1. The illustration of specimen preparation

employed as the reference material, and the heating rate was 50 °C /min.

Characterizations of specimen

The phase of the specimen was characterized by XRD with Cu Kα radiation (λ = 1.5405 Å). The average crystallite size was determined by the Debye-Scherrer equation. Mass shrinkage is determined by calculating the ratio of the difference between the mass of the specimen before and after sintering to the mass before sintering. The bulk density and apparent porosity were measured by the Archimedes principle according to the ASTM C373-88.

The pore characteristic of the specimen, including surface area, pore volume, and pore distribution, was determined by nitrogen adsorption using SAA at a temperature of 250 °C with outgas time of 3 h and bath temperature of 273 K. Brunauer-Emmet-Teller (BET) was used to calculate the specific textural properties such as surface area and pore volume. Using the t-plot approach, the total adsorbed gas at relative pressure $P/P_0 = 0.99$ was used to represent the total pore volume, and the pore distribution was based on Barret-Joyner-Halenda (BJH) analysis.

SEM was used to examine the specimen's microstructures, which qualitatively indicated a grain size of 60 mesh; the quantitative analysis was also examined with energy dispersive analysis (EDX), and phase quantification was obtained from SEM-EDX maps by processing EDX area maps using Image JED-2300 software.

■ RESULTS AND DISCUSSION

TGA-DTA of Gel Casted Green Body Ceramic

TGA-DTA was used in the determination of heat treatment parameters, including the sintering temperature of gel casted green body ceramic, to explain the process that occurs in the sintering process so that a thermal analysis of clay and CS, along with CMC, is also carried out. The results are shown in Fig. 2. To simplify the analysis, the thermal properties of green body ceramic based on the TGA-DTA curve are divided into three stages.

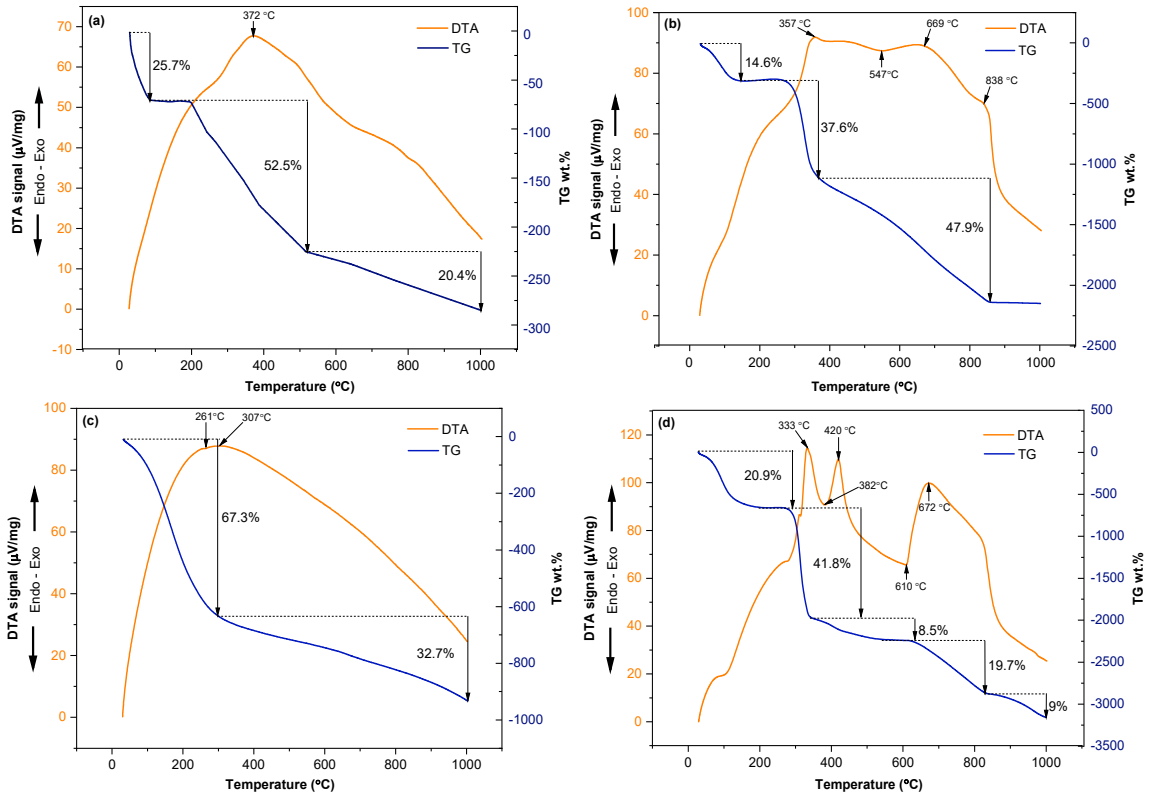

Fig 2. TGA-DTA curves of (a) gel casted green body ceramic, (b) CS, (c) clay, and (d) CMC

The first stage is the temperature increased from room temperature to 100 °C, and the mass of the green body decreased by about 25.7 wt.%, showing the removal of free and physically adsorbed water from the specimen's surface as well as the release of related water. In addition, it also indicates the evaporation of residual water in the CS polymer, which is in curve Fig. 2(b). There is also a reduction in mass at a temperature of 100 °C [37].

The second stage starts from 200 to 500 °C, the mass of the green body reduced to 52.5 wt.%. It is estimated that the hydration process of raw NC material occurs, which is in curve Fig. 2(c). There is also a reduction in mass at room temperature to 300 °C; this phenomenon is followed by a broad exothermic peak at 201 °C corresponding to the dehydroxylation of kaolinite into meta kaolinite [38]. Furthermore, curve Fig. 2(b). there was a decrease in mass at the temperature range of 200 to 400 °C, indicating the loss of the acetyl group that was still contained in the chitosan; the acetyl group had π bonding which is a weaker and more reactive bond so it was easier to break first. This phenomenon is followed by the exothermic peak at 357 °C, on the DTA curve [39]. It is estimated that at this stage, the formation of pores on the green body ceramic has started to occur.

The last stage is when the mass of the green body reduced to 20.5 wt.% from 500 to 1000 °C. This is due to the occurrence of degradation and decomposition of the CS chain, this is evidenced by the reduction in mass on the TGA curve of the CS thermogram (Fig. 2(b)), and there are also several small peaks which indicate the process of degradation and decomposition of various polymer units [39]. Thus, in this temperature range, it is suspected that the polymer network of CS will be burning out so that the formation of pores occurs optimally. In addition, at temperatures between 800 and 1000 °C, a massive DTA peak is visible; this is a result of the phase change from meta kaolin to Al-Si spinel [40].

In the sintering process, the mass reduction of CMC is only 20.9% at temperatures of 100 to 300 °C, which indicates water decomposition; at temperatures of 300 to 400 °C indicates CMC decomposition with a mass reduction of about 41.8%. Furthermore, mass reduction is not so significant at temperatures above 400 °C, which indicates the decomposition of cross-link bonds in CMC and confirms the occurrence of curing behavior in porous ceramic bodies [41]. In this study, CMC acts as a dispersant in the ceramic body so that its presence is bound to each other with the matrix and binder of the specimen [11]. Thus, based on the thermal properties of the green body ceramic, the thermal treatment applied to the porous ceramic specimen is shown in Fig. 3.

X-ray Diffraction Investigations

The gel casted green body ceramics was sintered with various sintering temperatures (900, 1000, and 1100 °C) and the mineral phases were identified by XRD (Fig. 4). The SiO_2 crystalline phase that appears for all specimens is quartz (JCPDS 46-1212) and cristobalite (JCPDS 39-1425), while the mullite phase is only found in specimens at a temperature treatment of 900 °C at 25.97° which corresponding to the plane of primary mullite phase [42]. In addition, there is also a corundum phase for all specimens. Corundum increases steadily in its amount, while quartz increases and the amount of corundum nearly disappears at 1000 °C; it is in contrast to the results of the previous study because the sintering temperature carried out in this study is lower than that which been done previously [40]. The appearance of

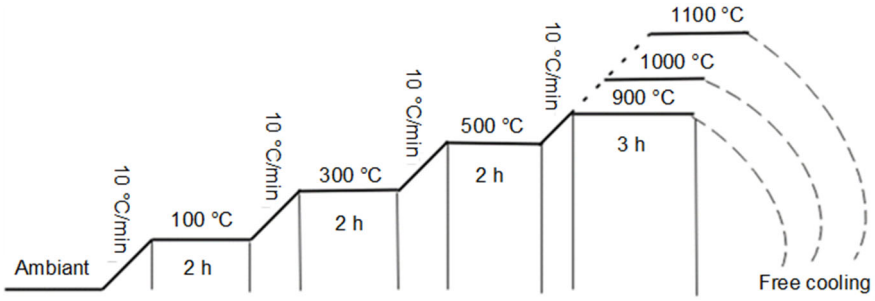

Fig 3. Thermal treatment applied in porous ceramic production

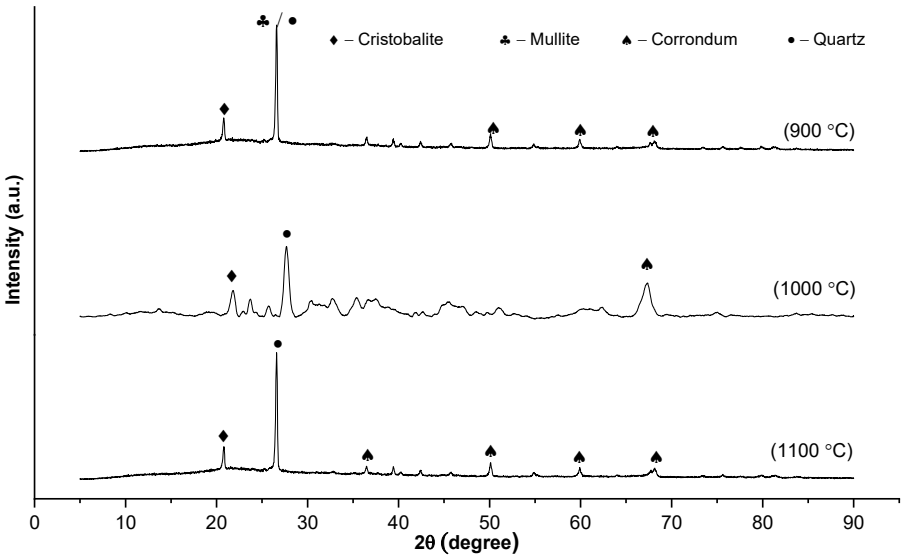

Fig 4. XRD patterns of the specimen with different sintering temperature

corundum peaks in all specimens indicates that not all alumina reacts with kaolinite in the clay to form mullite. The reason for failure to complete mullitization might be due to alumina size with large granular (18.64 μm) as raw material [25]. The results prove that the final phase compositions depend greatly on the treating temperatures.

The crystallinity of the specimen was determined by the Segal method. The weight fraction of the amorphous (x_A) component over different temperatures, was determined from Eq. (1) [43],

$$x_A(\%) = 100 - (1 - x_c) \quad (1)$$

where x_c is the crystallinity of the specimen given by Eq. (2) [43-44],

$$x_c(\%) = 100 \frac{I_{crystal}}{I_{crystal} + I_{amorphous}} \quad (2)$$

where $I_{crystal}$ and $I_{amorphous}$ correspond to the intensity of the integrated for all crystalline peaks and the amorphous scattering, respectively. The crystallinity of the specimen with different sintering temperatures is plotted in Fig. 5(b). Due to the microcline phase melting at a higher sintering temperature of 1000 °C, the crystallinity reduces, and the microstructure is typical of the sintering liquid phase. It was associated with the disappearance of the mullite phase (Fig. 4) due to the complete dissolution in the glass melt. This is agreed with the results of previous studies [45-46]. However, the crystallinity increased at 1100 °C, by reforming the diffraction peak; it was also known that the crystal diffraction peak and full width at half maxima (FWHM) did not change with increasing sintering temperature. Sintering temperature up to 1100 °C does not change the crystal phase but only causes an increase in the intensity of the diffraction peak [47].

Furthermore, the crystallite size (D) and the strain (ε) were obtained from three samples based on different thermal treatments. From the maximum peak FWHM amount, the crystallite size of specimens is calculated using the Debye-Scherrer equation as Eq. (3) [48], which takes from six data by taking the six dominant peaks as shown in Fig. 4 and the result is plotted in Fig. 5(a);

$$D = \frac{0.9\lambda}{\beta \cos\theta} \quad (3)$$

where β is the full width at half-maximum (FWHM) of the diffraction peak, λ (1.5406 Å) is the X-ray wavelength radiation of Cu Kα, and θ is the Bragg angle. Based on the Debye-Scherrer equation, shown in Table 2, the crystallite size of specimens decreased by the increasing sintering temperature from 900 to 1000 °C but increased homogenously at 1100 °C. This finding is different from the results of several previous studies, which revealed that the crystallite size increased with increasing sintering temperature with the same sintering temperature from 800 to 1000 °C [47,49-50]. This anomalous behavior can

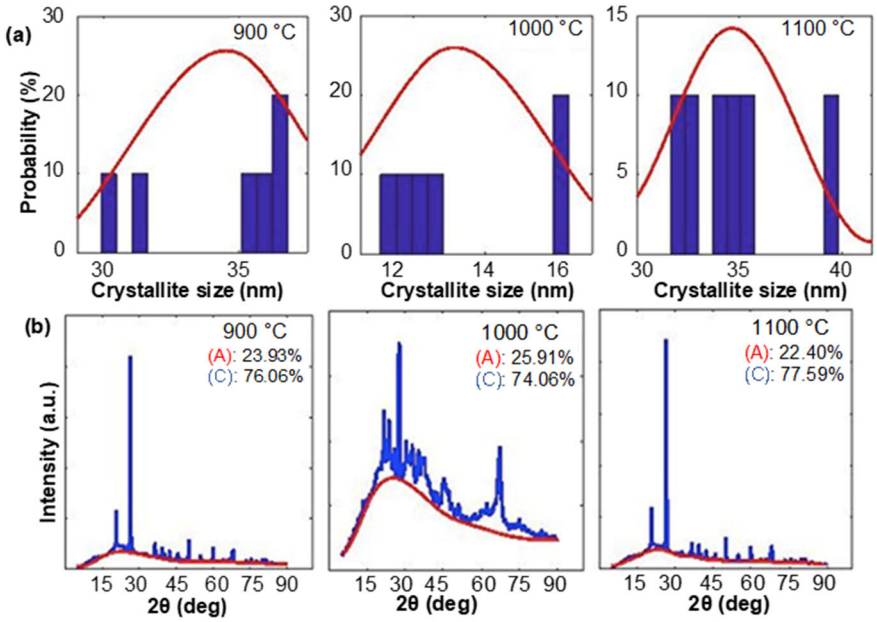

Fig 5. The evaluation of (a) the crystallite size of the specimens and (b) crystallinity with (A) amorphous and (C) crystalline phases

Table 2. The relationship between crystallite size and microstrains of the specimens

900 °C		1000 °C		1100 °C	
Crystallite size (nm)	Strain ($\times10^{-3}$)	Crystallite size (nm)	Strain ($\times10^{-3}$)	Crystallite size (nm)	Strain ($\times10^{-3}$)
31.45	6.63	16.34	12.16	33.87	6.18
35.61	4.60	15.93	9.89	32.96	4.98
36.38	3.40	12.45	9.98	35.07	3.44
36.78	2.42	11.56	7.60	39.84	2.24
35.71	2.12	12.35	5.89	34.47	2.19
29.87	2.26	11.07	6.16	31.67	2.13

be explained by assuming that a high defect concentration is produced during densification at 1000 °C; it can be attributed to the low crystallinity of the specimen at a sintering temperature of 1000 °C (Fig. 5) and associated rapid particle deformation [51]. In order to confirm the structural parameters of the specimens, the Williamson-Hall was also used to determine the strain using Eq. (4) [52]. The microstrains can be caused by dislocations, anti-phase domain borders, deformation faulting, or homogeneous crystal lattice distortion [53].

$$\beta hkl\cos\theta = k\alpha/D + (4\varepsilon\sin\theta) \quad (4)$$

When using the Williamson-Hall calculation method, it is presumed that the strain is constant throughout the crystallographic space and that the material's characteristics are independent of space [44]. Based on Table 2, the strain has a positive value, indicating the strain tensile present during the sintering process of gel casted green body ceramics. Thus, the crystallite coalescence occurs as a consequence of the destroying-rebuilt oxygen-metallic cation of quartz and corundum, regardless of the phase transition of quartz to cristobalite [54]. As previously mentioned, the crystal size increases with a sintering temperature of 1100 °C. It can be seen from the decrease in FWHM of the diffraction peak with the sintering temperature, indicating an increase in the crystallization process by eliminating defects such as crystal growth and coalescence. The findings are in agreement with the previous studies [47,55].

Pore Parameters of Sintered Specimens

Mass shrinkage, bulk density and apparent porosity

The effect of thermal treatment on the mass shrinkage, bulk density and apparent porosity of the sintered specimens are shown in Table 3. As the sintering temperature increased from 900 to 1000 °C, the mass shrinkage of specimens increased and decreased at 1100 °C. The mass shrinkage increased as a result of the interconnectedness of the kaolin grains in the specimen body becoming weirder with an increase in sintering temperature [56]. However, at the sintering temperature of 1100 °C, mass shrinkage decreased due to forming a large amount of glassy phase, supported by XRD data (Fig. 4); grain merging was not completed due to the very high intensity of quartz peaks.

Similar results were observed for apparent porosity and bulk density; as the sintering temperature increased from 900 to 1000 °C, porosity increased while density decreased. As the sintering temperature was 1100 °C, the porosity decreased, and density decreased. It means the mixture of kaolinite and corundum sinter maximally when fired at 1000 °C; it can also be learned from the highest mass shrinkage occurred at these conditions and the porosity of the porous ceramic is dependent on the temperature treatment. The density and porosity with various sintering temperatures were not so much different, and it was connected to the minor mass decrease. The results obtained are different from previous studies, which produce a regular trendline of the effect of the sintering temperature on density and porosity [56]. This is presumably because this study did not control the amount of alumina mixture as the raw material. Moreover, the resulting porosity is almost the same as the porous ceramic synthesized by conventional methods [33]. The findings suggest that by varying the sintering temperature, the bulk density and apparent porosity should be controllable.

Surface area, pore volume, and pore distribution

The surface area, pore volume, and pore distribution of the specimens were analyzed using the BET and BJH methods, shown in Fig. 6. As it is shown in the N_2 adsorption-desorption isotherms curves of specimens (Fig. 6(a)), no obvious hysteresis loops exist. After analyzing the BET data, the adsorption isotherm of the specimens is included in one of the types of adsorption isotherms discussed by Brunauer et al. [57],

Table 3. Mass shrinkage, bulk density, and apparent porosity with different sintering temperatures

Sintering temperature (°C)	Apparent porosity (%)	Bulk density (g/cm³)	Mass shrinkage (%)
900	30.14 ± 0.14	10.61 ± 0.01	4.18 ± 0.03
1000	37.82 ± 0.19	8.64 ± 0.03	5.74 ± 0.05
1100	29.96 ± 0.15	12.27 ± 0.01	4.01 ± 0.05

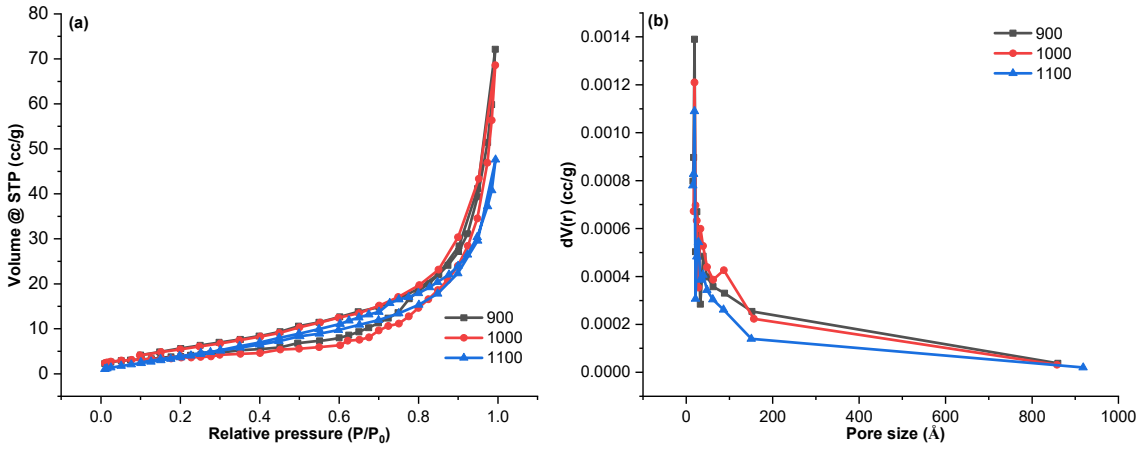

Fig 6. (a) Isotherm of adsorption-desorption curves and (b) pore size distribution of specimens

which is included in type III. This particular isotherm is convex to the axis of the relative pressure and does not show adsorption limiting $P/P_0 = 1$. When the adsorbate interacts more with the adsorbed layer than the adsorbent surface, type III isotherms are created.

The value of the surface area of the specimens increased from a temperature of 900 °C to a temperature of 1000 °C and decreased at a temperature of 1100 °C, while the volume and pore distribution of the specimens were not much different. The largest surface area occurs at a sintering temperature of 1000 °C, which is 17.27 m^2/g. The same results were observed by Akhtar et al. [58], which uses diatomite as a raw material; at temperatures above 1000 °C the surface area of the specimen decreases, which is associated with the formation of a melting phase at temperatures above 1000 °C which promotes liquid phase sintering. However, the surface area of the resulting porous ceramics is larger than that of the porous alumina ceramics synthesized by the freeze-drying [59] and wet-spun fibers method that also uses CS as a pore template [30]. During the sintering process, the grains agglomerate, resulting in a decrease in the pore volume, and the surface area of the ceramic powder decreases drastically [60-61]. The resulting pore distribution ranges from 19.1 Å, with the result that the porous ceramic is close to the mesoporous character. The pore characteristics of the specimens are summarized in Table 4.

Surface morphology of specimens

The SEM photographs for the fracture surface of specimens with various sintering temperatures are shown in Fig. 7. It was obvious that the specimens made through the gel casting method had complex microstructures, with large spherical pores containing microscopic cellular pores on their inside walls. The

Table 4. Pore characteristics of porous ceramic-based NC and CS correspond to Fig. 6

Sintering temperature (°C)	Surface area (m^2/g)			Volume @STP (cc/g)			[g]Pore distribution (Å)	
	[a]BET	[b]Micro	[c]Meso	[d]Total	[e]Micro	[f]Meso	Micro	Meso
900	15.2204	14.1493	1.0711	0.1116	0.0004	0.1111	19.0929	45.0112
1000	17.2752	9.0612	8.2140	0.0736	0.0041	0.0695	19.1011	37.2112
1100	12.5215	2.6483	9.8732	0.1061	0.0020	0.1041	19.1012	27.0001

[a]BET surface area; [b]Micropore surface area evaluated by *t*-plot method; [c]Mesopore surface area calculated using S_{BET}-S_{micro}; [d]Total pore volume at P/P_0 ~0.99; [e]Micropore volume calculated by t-plot method; [f]Mesopore volume calculated using V_{total}-V_{micro}; [g]Pore distribution based on BJH analysis

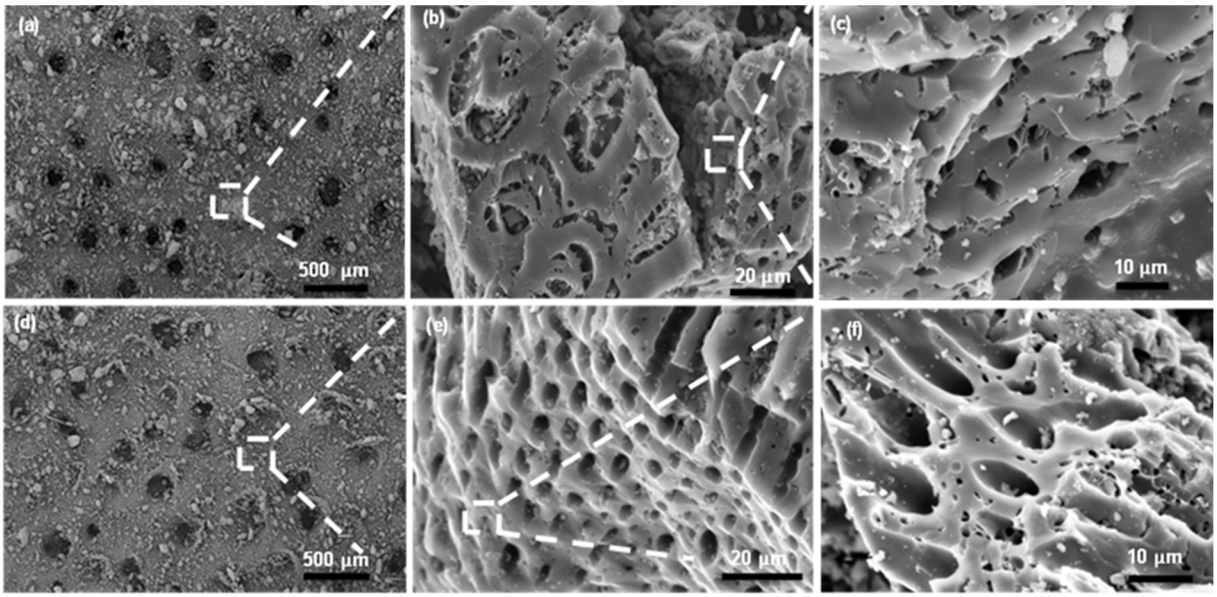

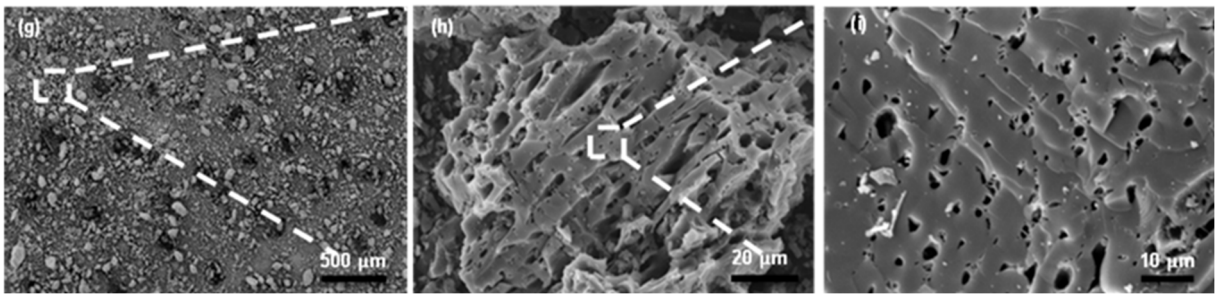

Fig 7. SEM images of the specimens with various sintering temperatures: 900 °C (a, b and c), 1000 °C (d, e and f), and 1100 °C (g, h and i)

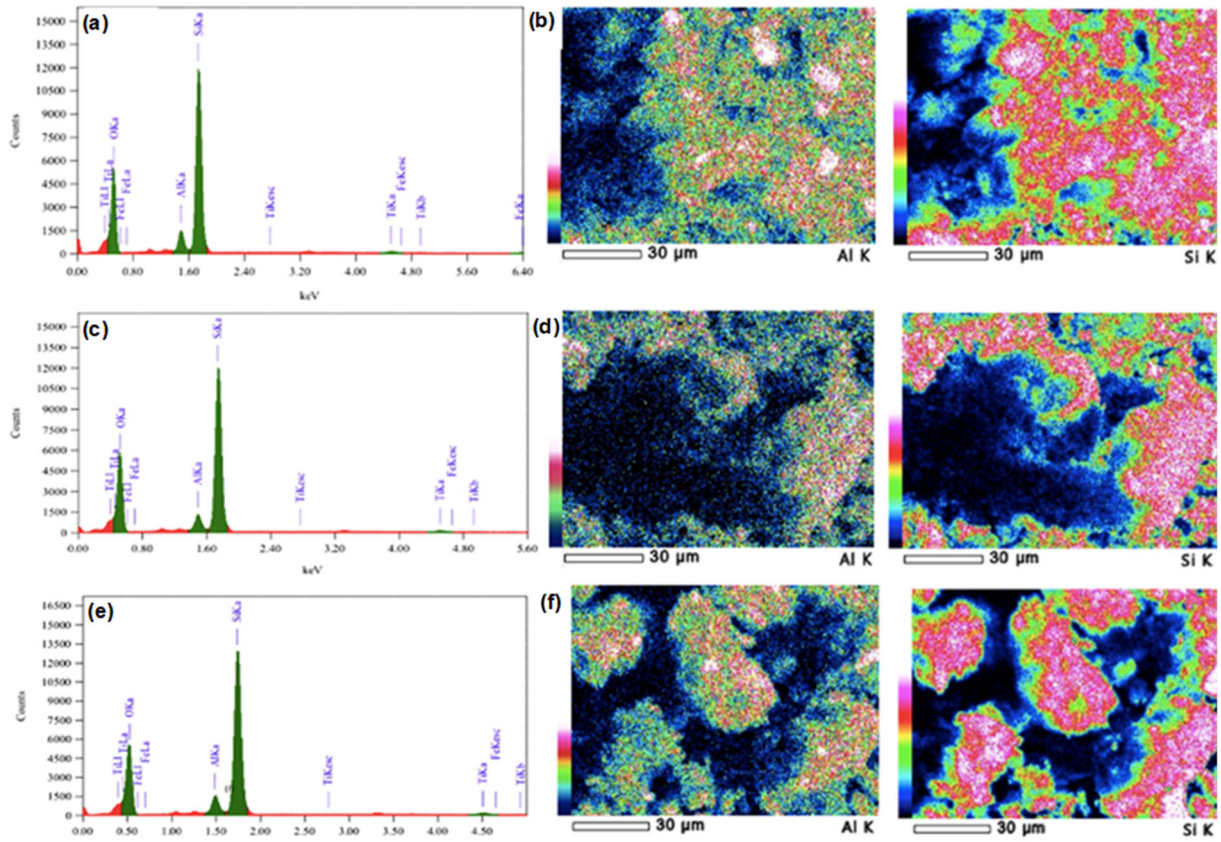

Fig 8. EDS elemental mapping of the specimens for sintering temperatures (a, b) 900 °C, (c, d) 1000 °C, and (e, f) 1100 °C

process of gelification produced large spherical pores, while the removal of CS and aggregation of quartz particles produced small cellular pores in internal walls [56]. It may be explained by mass shrinkage and porosity, which increase with increasing sintering temperature, that the number of small pores reduces as the sintering temperature increases from 900 to 1000 °C, as shown in Table 3. But when the sintering temperature is as high as 1100 °C, the porosity decreases drastically (Fig. 7(g, h, and i)), presumably due to the glass phases being less viscous and easy to flow, so they could fill most of the pores formed by burning the gel CS polymer and thereby dramatically reduce porosity. A similar result was observed by Liu et al. [40] reporting when the sintering temperature was increased, the large particles did not seem to fully fuse with each other, thus causing the porosity to decrease. Besides, Yang et al. [56] also observed at a certain high temperature, the growth and

Table 5. Elemental analysis of the specimens corresponds to Fig. 8 (a, c, and e)

Element	Compound	Mass (%) of element			Mol (%) of compounds		
		900 °C	1000 °C	1100 °C	900 °C	1000 °C	1100 °C
O K	-	52.06	52.02	52.25	-	-	-
Al K	Al_2O_3	4.50	4.17	3.79	8.50	7.88	7.17
Si K	SiO_2	41.24	41.31	42.09	88.22	88.38	90.04
Ti K	TiO_2	1.17	1.38	1.02	1.95	2.30	1.71
Fe K	Fe_2O_3	1.04	1.12	0.85	1.34	1.44	1.09

interconnection of kaolinite grains on the raw material were not uniform, causing the porosity to decrease. Surface morphology showing homogeneous pore distribution observed at a sintering temperature of 1000 °C which is shown in Fig. 7(d, e, and f).

To observe the distribution of Si and Al elements (which are the main constituents of NC) in sintered ceramics, an EDS mapping analysis was also carried out on the specimens, which is shown in Fig. 8. The results obtained showed an incomplete solid-state reaction, where the distribution of Si and Al elements was unevenly distributed equally. If it is associated with the pore size of the specimens in Table 4, where the smallest pore size occurs at a sintering temperature of 1000 °C, as shown in Fig. 8(d), the distribution of Al and Si elements is the most uneven among other treatments. It indicates that grain merging was not completed so grain growth was not completed during the sintering process, which only for 3 h, thus, the pores formed were smaller than other specimens [60]. The mass (%) of Si and mole (%) of compounds SiO_2 increases with increasing sintering temperature. Different results were observed for the element Al and its compounds showing the mass (%), and mole (%) decreased with increasing sintering temperature, as shown in Table 5.

■ CONCLUSION

Porous ceramics were formed by the gel casting method using NC and CS. Pore development was mostly brought about by CS's thermal degradation. The crystallinities of the ceramic decreased (76.06 to 74.06%) at sintering temperatures 900 to 1000 °C while the crystallite size decreased and the lattice strain increased. The apparent porosity increased (30.14 to 37.82%) at sintering temperature from 900 to 1000 °C. However, the apparent porosity decrease became 29.96% when the sintering temperature increased to 1100 °C, as indicated by the formation of heterogeneous microstructure was observed. The resulting pore size for all temperature treatments was almost mesoporous (19.1 Å). The findings imply that the sintering temperature can be used to continually regulate the microstructure behavior of porous ceramics based on NC and CS.

■ ACKNOWLEDGMENTS

The researcher would like to thank the Chemical Physics Laboratory of Hasanuddin University and Research Laboratory of Universitas Negeri Makassar that have supported and assisted in conducting the research.

■ AUTHOR CONTRIBUTIONS

Suriati Eka Putri conducted the experiment and wrote the manuscript, Ahyar Ahmad and Indah Raya revised the manuscript, Rachmat Triandi Tjahjanto and Rizal Irfandi did proofread the manuscript, Abd Rahman conducted the TGA/DTA and XRD analysis, Susilo Sudarman Desa conducted the BET and BJH calculations, Harningsih Karim did the grammar check process. All authors agreed to the final version of this manuscript.

■ REFERENCES

[1] Gopi, S., Pius, A., and Thomas, S., 2020, *Handbook of Chitin and Chitosan: Composites and Nanocomposites from Chitin and Chitosan, Manufacturing and Characterisations*, vol. 2, Elsevier, Amsterdam, Netherlands.

[2] Aouadja, F., Bouzerara, F., Guvenc, C.M., and Demir, M.M., 2021, Fabrication and properties of novel porous ceramic membrane supports from the

(Sig) diatomite and alumina mixtures, *Bol. Soc. Esp. Ceram. Vidrio*, 61 (5), 531–540.

[3] Guo, W., Hu, T., Qin, H., Gao, P., and Xiao, H., 2021, Preparation and in situ reduction of Ni/SiC_xOy catalysts supported on porous SiC ceramic for ethanol steam reforming, *Ceram. Int.*, 47 (10, Part A), 13738–13744.

[4] Han, L., Deng, X., Li, F., Huang, L., Pei, Y., Dong, L., Li, S., Jia, Q., Zhang, H., and Zhang, S., 2018, Preparation of high strength porous mullite ceramics *via* combined foam-gelcasting and microwave heating, *Ceram. Int.*, 44 (12), 14728–14733.

[5] Manap, N.R.A., and Jais, U.S., 2009, Influence of concentration of pore forming agent on porosity of SiO_2 ceramic from rice husk ash, *Mater. Res. Innovations*, 13 (3), 382–385.

[6] de Morais Santos, L.N.R., de Melo Cartaxo, J., Silva, J.R.S., Rodrigues, A.M., de Andrade Dantas, E.L., de Sousa, F.B., de Araújo Neves, G., and Menezes, R.R., 2021, High porous ceramics with isometric pores by a novel saponification/gelation/freeze-casting combined route, *J. Eur. Ceram. Soc.*, 41 (14), 7111–7118.

[7] Nishihora, R.K., Rachadel, P.L., Quadri, M.G.N., and Hotza, D., 2018, Manufacturing porous ceramic materials by tape casting—A review, *J. Eur. Ceram. Soc.*, 38 (4), 988–1001.

[8] Wang, X., Xie, Y., Peng, C., Wang, R., Zhang, D., and Feng, Y., 2019, Porous alumina ceramic via gelcasting based on 2-hydroxyethyl methacrylate dissolved in *tert*-butyl alcohol, *Trans. Nonferrous Met. Soc. China*, 29 (8), 1714–1720.

[9] Putri, S.E., Pratiwi, D.E., Tjahjanto, R.T., Mardiana, D., and Subaer, S., 2018, On the effect of acrylamide and methylenebicacrylamid ratio on gelcasted ceramic pore character, *J. Chem. Technol. Metall.*, 53 (5), 841–844.

[10] Hooshmand, S., Nordin, J., and Akhtar, F., 2019, Porous alumina ceramics by gel casting: Effect of type of sacrificial template on the properties, *Int. J. Ceram. Eng. Sci.*, 1 (2), 77–84.

[11] Dong, J., Wei, J., Han, L., Li, X., Han, B., and Yan, W., 2022, Preparation of porous halloysite nanotube ceramics with high porosity and low thermal conductivity by foam-gelcasting, *Ceram. Int.*, 48 (2), 2441–2448.

[12] Lukacs, V.A., Stanculescu, R., Curecheriu, L., Ciomaga, C.E., Horchidan, N., Cioclea, C., and Mitoseriu, L., 2020, Structural and functional properties of $BaTiO_3$ porous ceramics produced by using pollen as sacrificial template, *Ceram. Int.*, 46 (1), 523–530.

[13] Wei, J., Han, B., Wei, Y., Li, N., and Miao, Z., 2021, Influence of phase evolution and thermal decomposition kinetics on the properties of zircon ceramic, *Ceram. Int.*, 47 (19), 27285–27293.

[14] Fakhruddin, A.K., and Mohamad, H., 2018, Effect of glutinous rice flour and dried egg white in fabrication of porous cordierite by gel casting method, *Cerâmica*, 64 (370), 242–247.

[15] He, X., Su, B., Zhou, X., Yang, J., Zhao, B., Wang, X., Yang, G., Tang, Z., and Qiu, H., 2011, Gelcasting of alumina ceramics using an egg white protein binder system, *Ceram.-Silik.*, 55 (1), 1–7.

[16] Wan, W., Huang, C., Yang, J., and Qiu, T., 2014, Study on gelcasting of fused silica glass using glutinous rice flour as binder, *Int. J. Appl. Glass Sci.*, 5 (4), 401–409.

[17] Kanlai, K., Wasanapiarnpong, T., Wiratphinthu, B., and Serivalsatit, K., 2018, Starch consolidation of porous fused silica ceramics, *J. Met., Mater. Miner.*, 28 (1), 71–76.

[18] Luchese, C.L., Spada, J.C., and Tessaro, I.C., 2017, Starch content affects physicochemical properties of corn and cassava starch-based films, *Ind. Crops Prod.*, 109, 619–626.

[19] Putri, S.E., Pratiwi, D.E., Tjahjanto, R.T., Hasri, H., Andi, I., Rahman, A., Ramadani, A.I.W.S., Ramadhani, A.N., Subaer, S., and Fudholi, A., 2022, The renewable of low toxicity gelcasting porous ceramic as Fe_2O_3 catalyst support on phenol photodegradation, *Int. J. Des. Nat. Ecodyn.*, 17 (4), 503–511.

[20] Salomão, R., Cardoso, P.H., and Brandi, J., 2014, Gelcasting porous alumina beads of tailored shape and porosity, *Ceram. Int.*, 40 (10, Part B), 16595–16601.

[21] Brandi, J., Ximenes, J.C., Ferreira, M., and Salomão, R., 2011, Gelcasting of alumina-chitosan beads, *Ceram. Int.*, 37 (4), 1231–1235.

[22] Wu, J.M., Ma, Y.X., Chen, Y., Cheng, L.J., Chen, A.N., Liu, R.Z., Li, C.H., Shi, Y.S., and Lin, J.P., 2019, Preparation of Si_3N_4 ceramics by aqueous gelcasting using non-toxic agar powder as gelling agent without cooling crosslink process, *Ceram. Int.*, 45 (16), 20961–20966.

[23] Putri, S.E., Pratiwi, D.E., Triandi, R., Mardiana, D., and Side, S., 2018, Performance test of gelcasted porous ceramic as adsorbent of azo dyes, *J. Phys.: Conf. Ser.*, 1028, 012039.

[24] Yao, Q., Zhang, L., Chen, H., Gao, P., Shao, C., Xi, X., Lin, L., Li, H., Chen, Y., and Chen, L., 2021, A novel gelcasting induction method for YAG transparent ceramic, *Ceram. Int.*, 47 (3), 4327–4332.

[25] Liu, Y.F., Liu, X.Q., Li, G., and Meng, G.Y., 2001, Low cost porous mullite-corundum ceramics by gelcasting, *J. Mater. Sci.*, 36 (15), 3687–3692.

[26] Georgiev, A., Yoleva, A., and Djambazov, S., 2018, Influense of brewery waste sludge containing diatomite on the physical properties and thermal conductivity of porous clay bricks, *J. Chem. Technol. Metall.*, 53 (6), 1117–1122.

[27] Alves Xavier, L., de Oliveira, T.V., Klitzke, W., Mariano, A.B., Eiras, D., and Vieira, R.B., 2019, Influence of thermally modified clays and inexpensive pore-generating and strength improving agents on the properties of porous ceramic membrane, *Appl. Clay Sci.*, 168, 260–268.

[28] Rajiv Gandhi, M., Viswanathan, N., and Meenakshi, S., 2010, Preparation and application of alumina/chitosan biocomposite, *Int. J. Biol. Macromol.*, 47 (2), 146–154.

[29] Salomão, R., and Brandi, J., 2013, Filamentous alumina-chitosan porous structures produced by gelcasting, *Ceram. Int.*, 39 (7), 7751–7757.

[30] Salomão, R., and Brandi, J., 2013, Macrostructures with hierarchical porosity produced from alumina-aluminum hydroxide-chitosan wet-spun fibers, *Ceram. Int.*, 39 (7), 8227–8235.

[31] Bengisu, M., and Yilmaz, E., 2002, Gelcasting of alumina and zirconia using chitosan gels, *Ceram. Int.*, 28 (4), 431–438.

[32] Bouazizi, A., Breida, M., Karim, A., Achiou, B., Ouammou, M., Calvo, J.I., Aaddane, A., Khiat, K., and Younssi, S.A., 2017, Development of a new TiO_2 ultrafiltration membrane on flat ceramic support made from natural bentonite and micronized phosphate and applied for dye removal, *Ceram. Int.*, 43 (1, Part B), 1479–1487.

[33] Mouiya, M., Bouazizi, A., Abourriche, A., El Khessaimi, Y., Benhammou, A., El hafiane, Y., Taha, Y., Oumam, M., Abouliatim, Y., Smith, A., and Hannache, H., 2019, Effect of sintering temperature on the microstructure and mechanical behavior of porous ceramics made from clay and banana peel powder, *Results Mater.*, 4, 100028.

[34] Putri, S.E., Ahmad, A., Raya, I., Tjahjanto, R.T., and Irfandi, R., 2022, Synthesis and antibacterial activity of chitosan nanoparticles from black tiger shrimp shell (*Penaeus monodon*), *Egypt. J. Chem.*, Article in Press.

[35] Lei, M., Huang, W., Sun, J., Shao, Z., Duan, W., Wu, T., and Wang, Y., 2020, Synthesis, characterization, and performance of carboxymethyl chitosan with different molecular weight as additive in water-based drilling fluid, *J. Mol. Liq.*, 310, 113135.

[36] Sembiring, S., Simanjuntak, W., Situmeang, R., Riyanto, A., and Karo-Karo, P., 2017, Effect of alumina addition on the phase transformation and crystallisation properties of refractory cordierite prepared from amorphous rice husk silica, *J. Asian Ceram. Soc.*, 5 (2), 186–192.

[37] Szymańska, E., and Winnicka, K., 2015, Stability of chitosan–A challenge for pharmaceutical and biomedical applications, *Mar. Drugs*, 13 (4), 1819–1846.

[38] Barry, K., Lecomte-Nana, G.L., Seynou, M., Faucher, M., Blanchart, P., and Peyratout, C., 2022, Comparative properties of porous phyllosilicate-based ceramics shaped by freeze-tape casting, *Ceramics*, 5 (1), 75–96.

[39] Gámiz-González, M.A., Correia, D.M., Lanceros-Mendez, S., Sencadas, V., Gómez Ribelles, J.L., and Vidaurre, A., 2017, Kinetic study of thermal degradation of chitosan as a function of deacetylation degree, *Carbohydr. Polym.*, 167, 52–58.

[40] Liu, Y.F., Liu, X.Q., Wei, H., and Meng, G.Y., 2001, Porous mullite ceramics from national clay produced by gelcasting, *Ceram. Int.*, 27 (1), 1–7.

[41] Zhang, J., Tan, L., Dong, H., Qu, W., and Zhao, J., 2022, Curing behavior of sodium carboxymethyl cellulose/epoxy/MWCNT nanocomposites, *RSC Adv.*, 12 (20), 12427–12435.

[42] Shin, C., Oh, S.H., Choi, J.H., Hwang, K.T., Han, K.S., Oh, S.J., and Kim, J.H., 2021, Synthesis of porous ceramic with well-developed mullite whiskers in system of Al_2O_3-kaolin-MoO_3, *J. Mater. Res. Technol.*, 15, 1457–1466.

[43] de Oliveira, L.S., de Oliveira Melquiades, M., da Costa Pinto, C., Trichês, D.M., and de Souza, S.M., 2020, Phase transformations in a NiTiGe system induced by high energy milling, *J. Solid State Chem.*, 281, 121056.

[44] Reddy, M.P., Shakoor, R.A., Mohamed, A.M.A., Gupta, M., and Huang, Q., 2016, Effect of sintering temperature on the structural and magnetic properties of $MgFe_2O_4$ ceramics prepared by spark plasma sintering, *Ceram. Int.*, 42 (3), 4221–4227.

[45] Amir, N., Tahir, D., and Heryanto, H., 2023, Synthesis, structural and optical characteristics of Fe_3O_4/activated carbon photocatalysts to adsorb pesticide waste, *J. Mater. Sci.: Mater. Electron.*, 34 (5), 445.

[46] Lu, J., Li, Y., Zou, C., Liu, Z., and Wang, C., 2018, Effect of sintering additives on the densification, crystallization and flexural strength of sintered glass-ceramics from waste granite powder, *Mater. Chem. Phys.*, 216, 1–7.

[47] Almasri, K.A., Sidek, H.A.A., Matori, K.A., and Mohd Zaid, M.H., 2017, Effect of sintering temperature on physical, structural and optical properties of wollastonite based glass-ceramic derived from waste soda lime silica glasses, *Results Phys.*, 7, 2242–2247.

[48] Heryanto, H., and Tahir, D., 2021, The correlations between structural and optical properties of magnetite nanoparticles synthesised from natural iron sand, *Ceram. Int.*, 47 (12), 16820–16827.

[49] Singh, L.K., Bhadauria, A., Jana, S., and Laha, T., 2018, Effect of sintering temperature and heating rate on crystallite size, densification behaviour and mechanical properties of Al-MWCNT nanocomposite consolidated via spark plasma sintering, *Acta Metall. Sin. (Engl. Lett.)*, 31 (10), 1019–1030.

[50] Venkatesh, D., Siva Ram Prasad, M., Rajesh Babu, B., Ramesh, K.V., and Trinath, K., 2015, Effect of sintering temperature on the micro strain and magnetic properties of Ni-Zn nanoferrites, *J. Magn.*, 20 (3), 229–240.

[51] Fauzi, F., Noviyanto, A., Fitriani, P., Wibowo, A., Sudiro, T., Aryanto, D., and Rochman, N.T., 2022, Silicon carbide/polysilazane composite: Effect of temperature on the densification, phase, and microstructure evolution, *Indones. J. Chem.*, 22 (2), 548–556.

[52] Bindu, P., and Thomas, S., 2014, Estimation of lattice strain in ZnO nanoparticles: X-ray peak profile analysis, *J. Theor. Appl. Phys.*, 8 (4), 123–134.

[53] Khotib, M., Soegijono, B., Zainal Alim Mas'ud, Z.A., and Nadjamoeddin, G.L., 2022, Growth, electronic structure, and electrochemical properties of cubic $BaTiO_3$ synthesized by low-pressure hydrothermal-assisted sintering, *Indones. J. Chem.*, 22 (1), 242–252.

[54] Cavalheiro, A.A., de Oliveira, L.C.S., and dos Santos, S.A.L., 2017, "Structural Aspects of Anatase to Rutile Phase Transition in Titanium Dioxide Powders Elucidated by the Rietveld Method" in *Titanium Dioxide*, Eds. Janus, M., IntechOpen, Rijeka, Croatia, 63–81.

[55] Saparuddin, D.I., Noor Hisham, N.A., Ab Aziz, S., Matori, K.A., Honda, S., Iwamoto, Y., and Mohd Zaid, M.H., 2020, Effect of sintering temperature on the crystal growth, microstructure and mechanical strength of foam glass-ceramic from waste materials, *J. Mater. Res. Technol.*, 9 (3), 5640–5647.

[56] Yang, F., Li, C., Lin, Y., and Wang, C.A., 2012, Effects of sintering temperature on properties of porous mullite/corundum ceramics, *Mater. Lett.*, 73, 36–39.

[57] Brunauer, S., Deming, L.S., Deming, W.E., and Teller, E., 1940, On a theory of the van der Waals adsorption of gases, *J. Am. Chem. Soc.*, 62 (7), 1723–1732.

[58] Akhtar, F., Rehman, Y., and Bergström, L., 2010, A study of the sintering of diatomaceous earth to produce porous ceramic monoliths with bimodal porosity and high strength, *Powder Technol.*, 201 (3), 253–257.

[59] Hu, S., Feng, B., Tang, X., and Zhang, Y., 2019, Porous alumina ceramics obtained by particles self-assembly combing freeze drying method, *Materials*, 12 (6), 897.

[60] Aytimur, A., Koçyiğit, S., and Uslu, İ., 2014, Calcia stabilized ceria doped zirconia nanocrystalline ceramic, *J. Inorg. Organomet. Polym. Mater.*, 24 (6), 927–932.

[61] Putri, S.E., Ahmad, A., Raya, I., Triandi, R., Natsir, H., Taba, P., and Karim, H., 2023, A review of the development of the gel casting method for porous ceramic fabrication, *Rasayan J. Chem.*, 16 (1), 48–60.